ARTICLE | Article in Press

Microwave coherent addition in waveguides by berry phase locking

Gal Goldstein · Yossi Oppenheim · Vladimir Kleiner · Erez Hasman · Elhanan Maguid

Received: 10 June 2026 / Accepted: 25 August 2026
© The Author(s) 2026

Abstract

Coherent addition of electromagnetic sources is essential for scaling radiation power and brightness beyond the limits of individual emitters. Yet achieving robust, continuous phase control in waveguide systems at high power remains a major challenge. Here, we demonstrate coherent combining of microwave sources in metallic waveguides using geometric (Berry) phase locking. By controlling the polarization evolution of circular-waveguide modes on a generalized Bloch sphere, we realize a compact, passive phase shifter based on a rotated dielectric birefringent metamaterial implemented with subwavelength gratings. The device provides deterministic, continuous phase control via Berry-phase accumulation while sustaining high electromagnetic fields. We experimentally demonstrate stable phase shifting up to 2.3 MW peak power and near-ideal coherent combining, achieving simultaneous doubling of output power and brightness. This work establishes a geometric-phase paradigm for high-power microwave control and coherent addition, providing a scalable route to phase-stable, high-brightness microwave systems.

Introduction

Coherent addition is a central strategy for generating high-power, high-brightness electromagnetic radiation, particularly in the high-power microwave (HPM) regime[1–4], where the required output power exceeds the capabilities of individual sources. Coherent combining can be implemented either in free space or within hollow metallic waveguides, the latter being especially attractive for HPM applications owing to their low insertion loss and exceptional power-handling capacity. In waveguide-based architectures, coherent addition typically relies on a power combiner together with a phase shifter at one input to establish and maintain phase locking. Phase locking mechanism ensures that the wavefronts of all separate sources' channels are completely synchronized in time and space to merge beams into a single, high-power, diffraction-limited beam, bypassing the damage thresholds of individual components. Existing high-power phase-shifting approaches—including mechanically tuned elements, mode-conversion structures, ferrite-based devices exploiting the Faraday effect, semiconductor-based tunable elements such as PIN diodes and varactors, and ferroelectric or liquid-crystal components—are limited by trade-offs among power handling, insertion loss, physical footprint relative to the wavelength, and the speed or continuity of phase control[5–7].

This Article in Press is shared early to give you faster access to new research. It is citable and carries a permanent DOI. The final edited version will replace it automatically.



https://doi.org/10.1038/s41598-026-69026-z

Published online: 04 November 2026

scientific reports

Phase shifts can be achieved by controlling the polarization state of light via Berry-phase accumulation, also known as the geometric phase, ϕ_g[8–10]. This concept enables spin-controlled phase modulation by exploiting the photon spin associated with the intrinsic angular momentum of left- and right-circularly polarized light. Dielectric Berry-phase metasurfaces (BPMs), composed of subwavelength dielectric gratings, have been demonstrated in free-space applications for precise polarization control[11–27]. Their all-dielectric construction offers both high-power resilience and a compact footprint. Subwavelength gratings act as effective layers of a uniaxial crystal[12,13,28], introducing strong anisotropy into the material. In particular, a binary one-dimensional grating is presented in Fig. 1(b) with subwavelength period Λ consisting of two alternating dielectric materials with permittivities ε_1 and ε_2 and widths t_1 and t_2 respectively, functions as a birefringent metamaterial. This inherent anisotropy allows the structure to operate as a zero-order retarder, enabling precise manipulation of the polarization state of the incident wave.

In free space, the polarization state is conventionally represented on the Poincaré sphere using an orthogonal basis of left- and right- circularly polarized states. Within metallic waveguides, the analog of circular polarization is realized through the linear superposition of two orthogonal linearly polarized degenerate modes. Circular waveguides naturally support such orthogonal modes due to their axial symmetry. In particular, the circularly polarized TE_{11} modes, TE_{11}^{+} and TE_{11}^{-}, can be expressed as $|TE_{11}^{\pm}\rangle = \left(|TE_{11}^{0^\circ}\rangle \pm i|TE_{11}^{90^\circ}\rangle\right)/\sqrt{2}$, where $|TE_{11}^{0^\circ}\rangle$ and $|TE_{11}^{90^\circ}\rangle$ are the orthogonal linearly polarized modes oriented at 0° and 90° relative to the x-axis of the waveguide cross-section. The circular polarization modes form an orthogonal basis for the waveguide modal states, such that any superposition can be written as $|a,b\rangle = a\,|TE_{11}^{+}\rangle + b\,|TE_{11}^{-}\rangle$.These states can be mapped onto a generalized Bloch sphere by the transformation, $a = \cos(\theta/2)$ and $b = e^{i\varphi}\sin(\theta/2)$, giving $\Psi = \cos\left(\frac{\theta}{2}\right)|TE_{11}^{+}\rangle + e^{i\varphi}\sin\left(\frac{\theta}{2}\right)|TE_{11}^{-}\rangle$, as illustrated in Fig. 1(c). This representation provides an intuitive geometric framework to describe the evolution of polarization states and the accumulation of Berry phase[29,30] in waveguide systems[31]. Note that Poincaré sphere can be regarded as a specific case of Bloch sphere for free space modes of polarized plane waves.

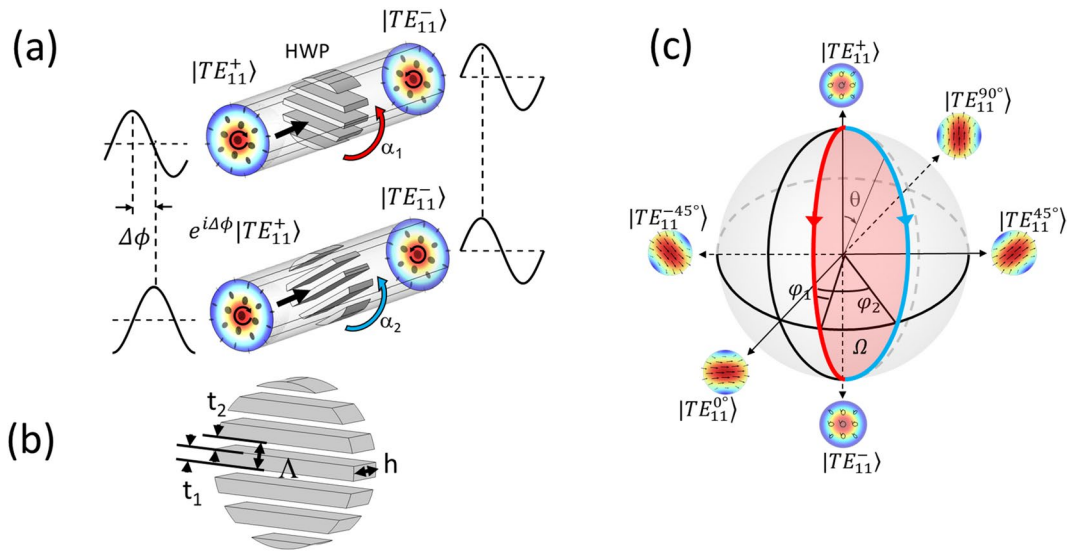


Fig. 1 Principle of coherent addition of two sources via Berry-phase accumulation. (a) Two circularly polarized waveguide mode sources are converted from $|TE_{11}^{+}\rangle$ to $|TE_{11}^{-}\rangle$ by half-waveplate birefringent phase modulators (HWP-BPMs). The orientations of the HWPs, α_1 and α_2 (red and blue arrows), induce Berry-phase accumulation that results in a net zero relative phase delay between the sources. (b) Schematic of the BPM structure, consisting of a dielectric uniaxial subwavelength grating with period Λ, dielectric ridge width t_1, air gap t_2, and retarder length (thickness), h, along the propagation direction. (c) Polarization transformations induced by the rotated BPMs, represented as geodesic trajectories on the generalized Bloch sphere. The azimuthal angles ϕ are related to the BPM rotation angles by $\phi_1 = 2\alpha_1$ (red arc) and $\phi_2 = 2\alpha_2$ (blue arc). The enclosed solid angle, Ω, corresponds to twice the difference in Berry-phase accumulation between the two sources.

The evolution of the waveguide modal state is visualized at Fig. 1(c) as a trajectory on the generalized Bloch sphere. Manipulation of this state is achieved using adiabatic operators, such as retardation and rotation. A retardation operator, which induces a geodesic transition between the north and south poles of the sphere, can be implemented with a half-wave plate (HWP). Rotation of the HWP around the axis of the waveguide by an angle α corresponds to an operator, which rotates the geodesic trajectory by 2α and thereby functions as a phase shifter through Berry-phase accumulation as illustrated in Fig. 1(a). The resulting geometric phase is equal to half of the solid angle Ω subtended by the trajectory on the Bloch sphere, such that $\phi_g = \Delta\phi = \Omega/2 = (\varphi_2 - \varphi_1) = 2(\alpha_2 - \alpha_1)$. This framework provides a direct and intuitive geometric interpretation of phase control in waveguide systems, linking modal evolution, polarization manipulation, and Berry-phase–mediated coherent addition.

Here we demonstrate coherent addition of two waveguide microwave sources mediated by geometric (Berry) phase accumulation, achieved through controlled evolution of waveguide-mode polarization on a generalized Bloch sphere. We introduce a high-power-resilient phase shifter based on a rotated dielectric BPM embedded in a single-mode circular waveguide, enabling deterministic phase control and coherent combining. This approach achieves simultaneous doubling of power and brightness of a waveguide mode relative to a single microwave source, establishing a geometric-phase paradigm for scalable, high-brightness high-power microwave systems.

Results

To realize Berry phase manipulation, we embedded a uniform, subwavelength BPM within a single-mode circular waveguide, where it interacts with the spatially varying polarization of the TE_{11} mode. On this basis, we designed and simulated alumina-based subwavelength binary gratings that function as π/2 and π retarders, corresponding to QWP and HWP, respectively. Figure 2 illustrates the polarization control achieved at an operating frequency of 2.856 GHz. The initial waveplate geometries were analytically determined using effective-medium theory, accounting for the guided wavelength within the circular waveguide. This preliminary design was subsequently refined using finite-element frequency-domain (FEFD) simulations to optimize the final BPM geometry.

The spatially varying input mode interacts with the uniform BPM retarder to yield high transmission accompanied by high-purity mode conversion, which is visualized in Fig. 2(a) and 2(b) as trajectories on the generalized Bloch sphere. We examine how a uniform BPM can coherently interact with a space-variant waveguide mode while preserving modal purity during propagation. Modal purity is quantified through spatial Stokes-parameter correlations between the ideal target mode and the obtained output modes, depicted at Fig. 2(c), 2(d) and 2(e) respectively. Using this approach, we achieve mode-conversion efficiencies exceeding 95% for both the QWP and HWP implementations.

The high modal purity arises from operation in a single-mode waveguide, which suppresses non-propagating higher-order modes and prevents their accumulation during propagation. The dominant interaction between the space-variant waveguide mode and the uniform BPM occurs in the central region of the mode, where the polarization is nearly uniform and the field intensity is maximal. By contrast, boundary-induced perturbations near the metallic walls primarily excite higher-order modes that carry negligible power, as the local intensity density (S_0) is minimal. Consequently, these contributions lead to only minor losses, resulting in high overall transmission efficiency.

The Berry phase shift is illustrated in Fig. 2(f) as a function of the HWP rotation angle, α, and is calculated as $\phi_g = arg\left(\langle\psi|HWP^{\dagger}(\alpha_2)|HWP(\alpha_1)|\psi\rangle\right)$, where $|\psi\rangle = |TE_{11}^{+}\rangle$ denotes the initial waveguide mode and $HWP(\alpha)$ represents the operator of a rotated HWP. The resulting phase shift closely follows the expected linear relation $\phi_g = 2\alpha$ while maintaining a high degree of spatial uniformity across the mode profile as shown in Fig. 2(f), insets. The spatial distribution of the geometric phase is nearly uniform in the central region of the waveguide, where the field intensity is highest, and exhibits deviations of up to ±2° near the metallic boundary. Because the intensity density is minimal in this boundary region, these deviations contribute negligibly to the net phase accumulation.

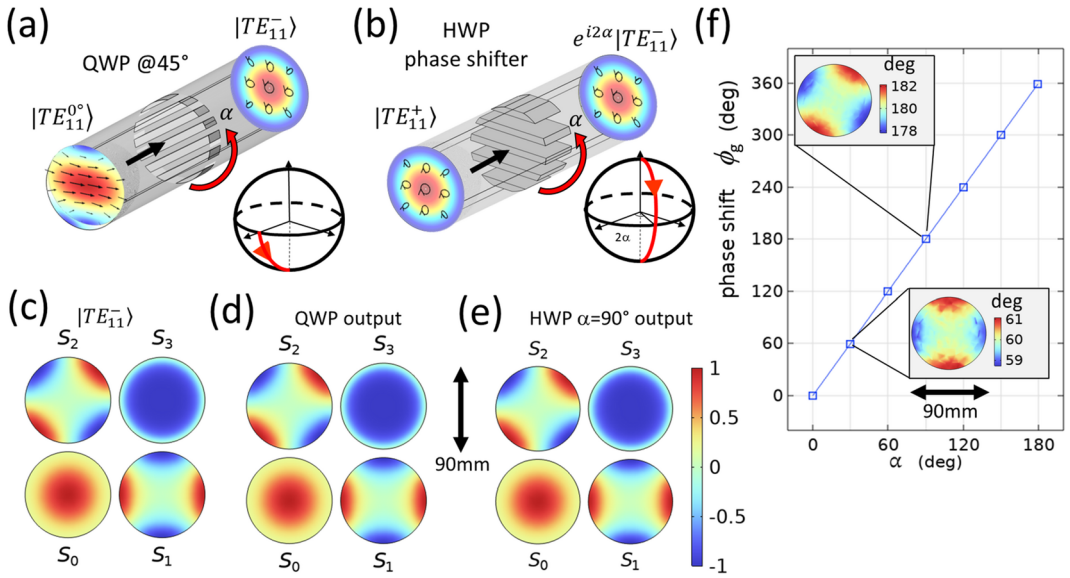


Fig. 2 Numerical simulation of BPMs in a circular waveguide. (a, b) Simulated input and output modes of a QWP (a) and HWP (b) BPM. Insets show the corresponding polarization-state transformations mapped onto the generalized Bloch sphere. The QWP converts the linearly polarized mode $|TE_{11}^{0^\circ}\rangle$ into left-handed circularly polarized mode $|TE_{11}^{-}\rangle$, whereas the HWP converts the right-handed mode $|TE_{11}^{+}\rangle$ into left-handed $|TE_{11}^{-}\rangle$ mode, accumulating a Berry phase that induces a phase shift of 2α. The QWP parameters are Λ = 14.8 mm, t_1 = 6.8 mm, t_2 = 8 mm, h = 14.8 mm and the HWP with Λ = 20 mm, t_1 = 7 mm, t_2 = 13 mm and h = 53.5 mm. Both structures are fabricated from alumina with relative permittivity ε_r = 9.9 and 90 mm diameter, same as the inner waveguide size. (c - e), Spatial Stokes parameters (S_0-S_3) comparing the ideal $|TE_{11}^{-}\rangle$ mode (c) with the QWP (d) and HWP (e) output modes. (f) Berry phase ϕ_g as a function of the BPM rotation angle α at f = 2.856 GHz. Insets show the spatial phase-shift distributions for α = 30° and α = 90°.

Together, these results demonstrate that the BPM structures function as highly efficient mode converters and spatially uniform phase shifters, combining high transmission efficiency with robustness suitable for high-power operation. For frequencies away from the design frequency, the retardation deviates from the ideal half-wave condition due to its approximately linear dependence on frequency. Consequently, the state evolution on the generalized Bloch sphere no longer reaches the antipodal point exactly, leading to an output field that is a superposition of the desired mode and the original input mode. Furthermore, filtering the desired mode, left-handed circularly polarized mode $|TE_{11}^{-}\rangle$, at the output preserves the target geometric phase response, at the cost of some reduction in efficiency. Therefore, the phase shifter for the desired mode has a broad bandwidth since geometric phase is achromatic, while maintaining the relation $\phi_g = 2\alpha$, as opposed to traditional phase shifters based on dynamic phase which are affected by frequency. The reduction in efficiency can be improved using achromatic retarder designs[32].

The mode-conversion efficiency of circular waveguide modes $|\psi\rangle = |TE_{11}^{\pm}\rangle$ propagating through a BPM is defined using an operator approach by $\eta = |(t_{0^\circ} - t_{90^\circ} e^{i\phi})/2|^2$[12,13], representing an effective modification of the free-space derivation. Figure 3b depicts the transmission coefficients, t_{0° and t_{90°, of the orthogonal linearly polarized modes, $|TE_{11}^{0^\circ}\rangle$ and $|TE_{11}^{90^\circ}\rangle$, within a circular waveguide. The approximation for the phase retardation, ϕ, between these modal states is defined by $\delta = \pi f_0/f$, where f_0 is the working frequency. For an ideal half-wave plate (HWP) BPM characterized by equal transmission magnitudes and a π phase retardation, 100% efficiency is achieved. The simulation shows maximum 93% conversion efficiency and a bandwidth of 300 MHz. Figure 3c illustrates the theoretical agreement between the operator-derived efficiency, η, and the numerically simulated circular mode conversion efficiency, $\eta^{\pm} = \langle TE_{11}^{\mp}|HWP|TE_{11}^{\pm}\rangle$, across this 300 MHz bandwidth. When the waveplate deviates from ideal parameters, the efficiency drops and an unaffected mode behaves as an intrinsic loss in the waveguided system. Unlike the analytical operator approach, the full-wave simulation rigorously accounts for

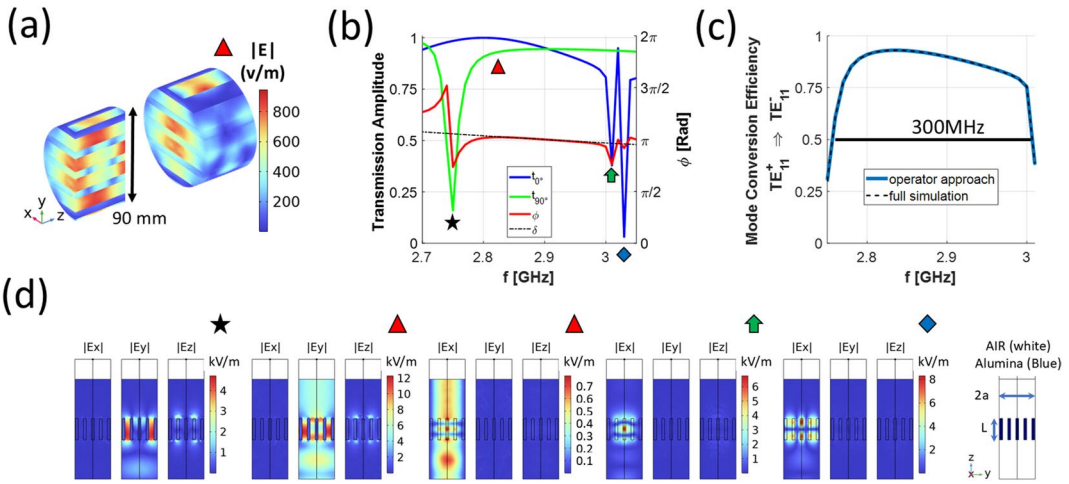


Fig. 3 Simulated conversion efficiency of a circular waveguide mode propagating through HWP BPM. (a) Full-wave simulation of the HWP-BPM at the operating frequency of 2.86 GHz under an incident $TE_{11}^{\pm}$ mode. (b) Transmission coefficients, t_{0° and t_{90° (left axis), alongside the phase retardation ϕ and its linear approximation, δ (right axis). (c) Calculated efficiency, η, evaluated from panel (b) (blue line) compared with the numerically simulated conversion efficiency between orthogonal circular modes, $\eta^{\pm}$ (black dashed line). The black horizontal line indicates the operational bandwidth. (d) Spatial electric field magnitude distributions at selected resonances (2.75, 3.01, and 3.03 GHz) compared to the optimal working frequency of 2.86 GHz. Resonances are marked by black star, green arrow and blue rhombus respectively, while working frequency of 2.86 GHz marked by two red triangles. The black star and left red triangle are excited by $|TE_{11}^{90^\circ}\rangle$ mode; the right red triangle and the green arrow and blue rhombus are excited by the $|TE_{11}^{0^\circ}\rangle$ mode.

waveguide boundary conditions and the continuous superposition of the circular mode propagating through the BPM.

Furthermore, the operational bandwidth is fundamentally constrained by structural resonances arising from the interaction between the incident waveguide mode and the waveplate's anisotropy. Figure 3d highlights that the optimal working frequency of the HWP resides between two distinct resonances, which couple to the $|TE_{11}^{0^\circ}\rangle$ and $|TE_{11}^{90^\circ}\rangle$ modes at different frequencies. The resonances originate from a macroscopic Fabry-Pérot across the entire metamaterial block, whereas the lower- and higher-frequency resonances correspond to transverse and longitudinal modes (marked by a black star and a blue rhombus, respectively).

To evaluate high-power durability, we simulated the electric field distribution at the operating frequency. As depicted in Fig. 3a, the peak electric field magnitude reaches 1 kV/m for 1 W of input power. This value scales to a theoretical breakdown limit of 10 MW in unpressurized air (1 atm) and 90 MW in an SF_6 environment, assuming an ideal waveguide geometry. In practice, these thresholds are reduced by manufacturing tolerances and the integration of standard RF line components (e.g., couplers, isolators, and gas inlets). Consequently, pressurization to 2 atm of SF_6 is standard protocol to sustain multi-megawatt operation.

Guided by numerical simulations, we fabricated metallic circular waveguide using a CNC technique and two alumina based QWPs; we experimentally verified a retardation of 90°, with measured transmission efficiencies exceeding 90% along both the slow and fast axes as shown in Fig. 4(a). Figure 4(b) illustrates the elements that were assembled into a compact phase-shifter architecture consisting of a stationary QWP oriented at 45°, which converts the input $|TE_{11}^{0^\circ}\rangle$ waveguide mode from linear to circular polarization, followed by a rotating QWP and a mirror. Note that the microwave source operated in the $|TE_{11}^{0^\circ}\rangle$ mode, coupled from a rectangular waveguide into a circular one. The rotating QWP–mirror combination functions as a Berry-phase phase-shifting element by exploiting the reflection symmetry of an HWP. The resulting double pass through the rotating QWP is topologically equivalent to the action of a rotated HWP, enabling continuous geometric-phase control within a short interaction length. This design yields a compact and efficient phase shifter that relies on a single BPM element.

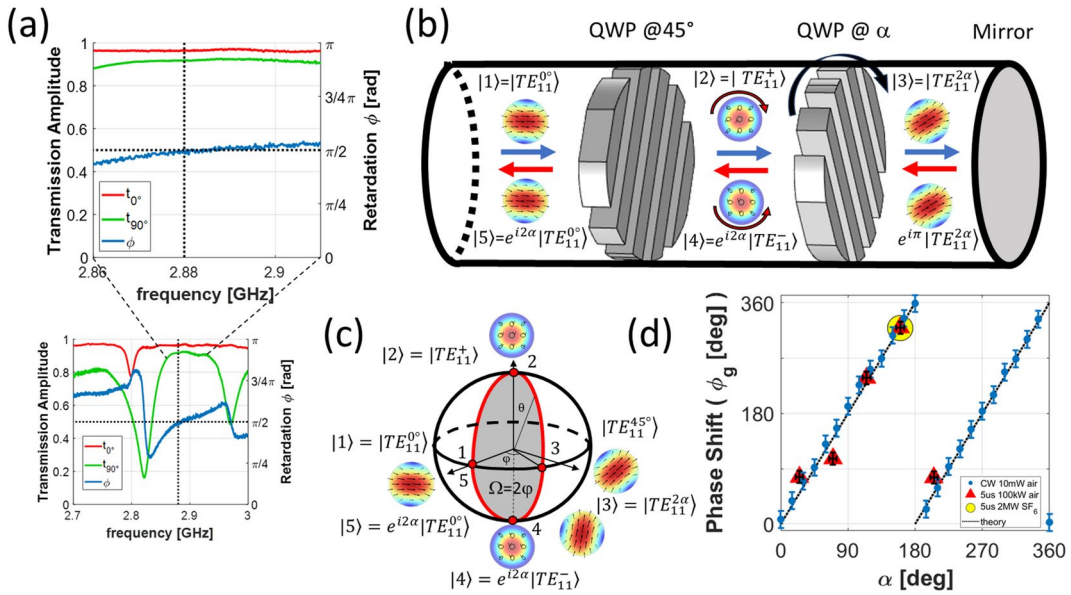


Fig. 4 Experimental demonstration of a compact Berry-phase shifter based on a QWP-BPM. (a) Experimental characterization of the QWP-BPM. Measured transmission coefficients along the slow (red) and fast (green) axes, and the corresponding phase retardation between the two axes (blue). A retardation of 90° is obtained at 2.88 GHz (black dashed lines), at which the device operates as a QWP. Inset (upper image) depicts the experimental characterization at the working frequency bandwidth. (b, c) Operating principle of the reflection-type Berry-phase shifter. (b) Mode evolution inside the phase shifter. Upper insets show the forward-propagating modes $|1\rangle$ to $|3\rangle$, while lower insets show the reflected backward-propagating modes $|4\rangle$ to $|5\rangle$. (c) Corresponding modes evolution represented as a trajectory (red curve) on the generalized Bloch sphere; discrete states $|1\rangle$ to $|5\rangle$ are indicated by red markers. (d) Measured phase shift as a function of rotation angle. Theoretical prediction is shown by the black dashed line. Experimental results are shown for low-power measurements (blue circles), and for high-power operation at 100 kW (red triangles) and 2.3 MW (yellow circle).

The evolution of the modal polarization state within the phase shifter is visualized in Fig. 4(c) as a trajectory on the generalized Bloch sphere. The evolution from the initial state $|1\rangle$ to the final state $|5\rangle$ traces a closed path, resulting in the accumulation of a Berry phase. This phase, ϕ_g equals half of the enclosed solid angle Ω and is equivalently twice the rotation angle α of the rotating QWP. As a result, the output state acquires a controllable phase shift of 2α such that $|5\rangle = e^{i2\alpha}|1\rangle$.

The performance of the reflection-based phase shifter was characterized across both low- and high- power regimes. Low-power measurements were carried out using a vector network analyzer with a 10 mW continuous-wave source, enabling phase-shift measurements with a resolution of 0.1° at the QWP operating frequency of 2.88 GHz. The measured phase response shows excellent agreement with theoretical predictions depicted by the blue symbols in Fig. 4(d). High-power operation was evaluated at 2.856 GHz using 5 µs pulses at a 50 Hz repetition rate. Under atmospheric pressure, the device sustained peak powers up to 100 kW without electrical breakdown, as confirmed across five fixed phase settings depicted by the red symbols in Fig. 4(d). By pressurizing the system with 10 psi of SF_6, the maximum peak power was extended to 2.3 MW which is depicted by the yellow symbol in Fig. 4(d), demonstrating stable phase control under extreme electromagnetic fields.

The experimentally observed breakdown threshold aligns well with expected field limits; while theoretical models predict breakdown limits in the tens of megawatts for perfect waveguides, practical power handling is typically restricted to the megawatt regime by standard inline components such as circulators and couplers. Furthermore, Fig. 5b illustrates that a conversion efficiency resonance is located near the measurement frequency (2.856 GHz). This proximity enhances the local electric field, which lowers the breakdown threshold to 15 MW at 1 atm of SF_6. The phase shifter efficiency, illustrated in Fig. 5b, was measured using a vector network analyzer and found to be 90%, demonstrating strong correlation with the full-wave simulation of the propagating

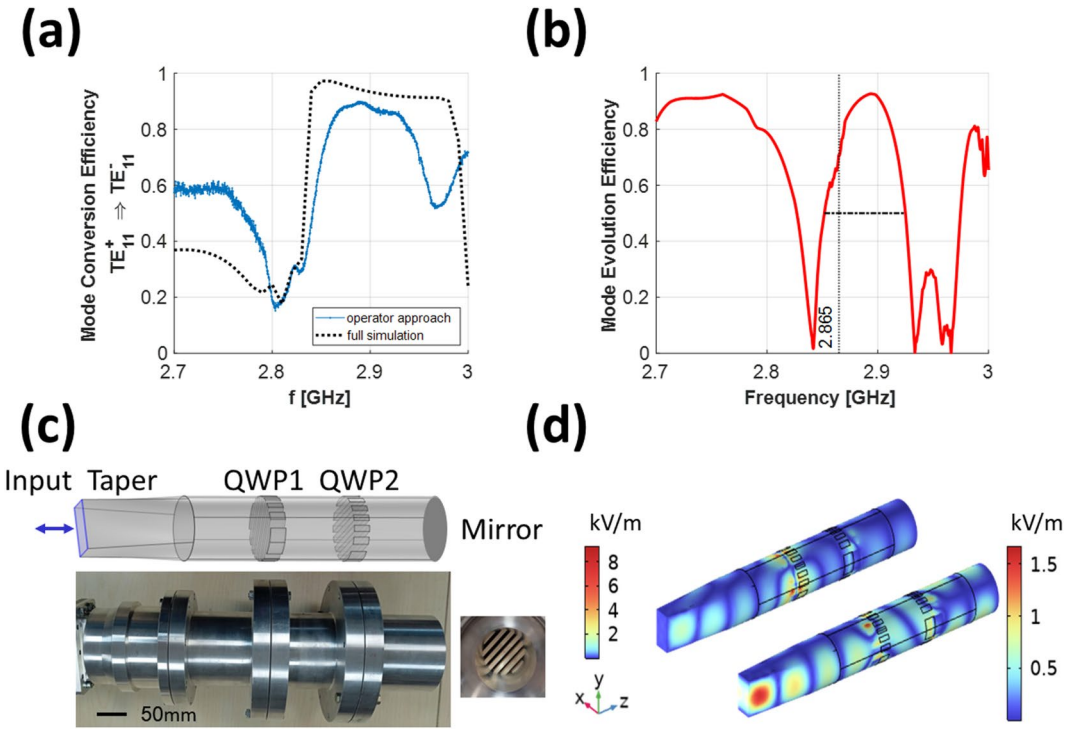


Fig. 5 Efficiency and characterization of the reflection-type Berry-phase shifter. (a) Experimental and simulated mode-conversion efficiency for a double pass through the QWP. (b) Measured overall efficiency of the Berry-phase shifter as a function of frequency. (c) Experimental low-power characterization setup. The top panel illustrates the 3D system design, while the bottom panel shows the assembled laboratory device. The right inset displays the BPM positioned inside the circular waveguide. (d) Full-wave FEFD simulations of the reflection-type Berry-phase shifter at the destructive resonance frequency (top) and at the optimal operating frequency (bottom).

and reflected modes. For high-power operation, an additional 1 dB insertion loss from the RF circulator must be accounted for.

The measured efficiency is in good agreement with the mode conversion efficiency of a double pass QWP (effective HWP in reflection) as depicted in Fig. 5a, whereas the observed resonances and reduced bandwidth in Fig. 5b are attributed to the multiple passes within the reflection-type phase shifter.

Figure 5d visualizes the full-wave simulation of the modal state evolution: the input $|TE_{11}^{0^\circ}\rangle$ mode is converted to a $|TE_{11}^{-}\rangle$ state by the stationary BPM (QWP1). The rotated BPM (QWP2) generates the $|TE_{11}^{2\alpha}\rangle$ state which is reflected by a metallic mirror into the $|TE_{11}^{-}\rangle$ state, acquiring a geometric phase shift of 2α. Finally, the first BPM converts the mode back to the linearly polarized $e^{i2\alpha}\,|TE_{11}^{0^\circ}\rangle$ state with the accumulated phase at the operating frequency. However, at a destructive resonance, the device does not operate as intended; consequently, the functional operating bandwidth of the Berry-phase shifter is fundamentally bound by these structural resonances

Figure 6(a) illustrates the phase shifter that was integrated with a waveguide power combiner via a circulator to demonstrate coherent addition of microwave sources. One source was coupled directly to one input of the combiner, while the second source was routed through the phase shifter, allowing precise control of the relative phase between the two inputs. Two experimental configurations were investigated. In the first, a single source was split into two coherent channels prior to recombination, establishing a baseline for ideal phase-controlled combining. Figure 6(b) shows the second configuration in which a common seeder drove two independent amplifiers, introducing uncorrelated noise in each channel and thereby providing a more stringent test of the robustness of the phase-control and coherent-combining scheme.

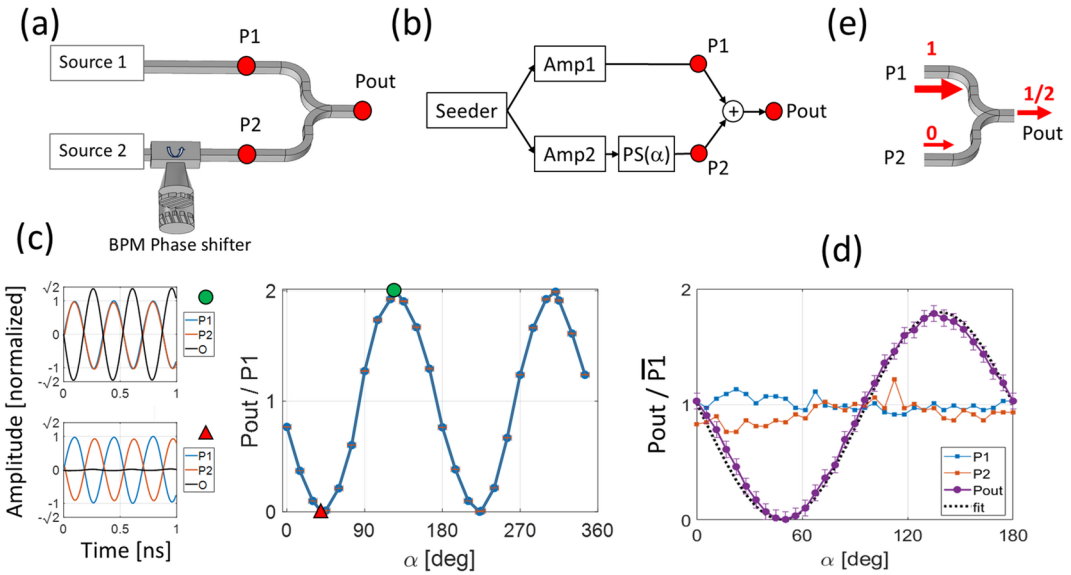


Fig. 6 Coherent combining of two microwave sources. (a, b) Experimental implementation of a two-way single mode rectangular waveguide power combiner (WR284, the dimensions cross-section of the rectangular waveguide 2.84 × 1.34 inches). The input ports P1, P2, and output port, Pout, are indicated by red markers. A reflection-type circular-waveguide Berry-phase shifter is integrated into the path of source 2 via a circulator and a rectangular-to-circular mode converter. (b) Seeder configuration feeding two amplifiers, intentionally introducing additional temporal and amplitude noise. (c) Measured output-to-input power ratio as a function of the phase-shifter rotation α, showing a maximum value of 1.978 (green marker). Insets show voltage measurements of the inputs P1, P2 and the output O, at two operating points, corresponding to destructive interference (residual output-to-input amplitude ratio of 0.018, red) and constructive interference (amplitude ratio of √2, green). (d) Output power ratio (purple), normalized to mean of P1, as a function of rotation angle α, exhibiting the expected cosine dependence despite excess noise in the individual input powers P1 (blue) and P2 (red). A maximum power ratio of 1.736 is achieved at 2.856 GHz. The power ratio error is ±0.07 and the rotation error is ±5°. A fit to sine curve (dotted black line) with an amplitude 0.9 and phase shift of −6.9° shows maximum ± 5% deviation from the measured power ratio. (e) Interferometric performance of the power combiner. With 1 W applied to P1 and P2 terminated, the measured 0.5 W output confirms design-compliant interferometric behavior.

When two waveguide modes, $|\psi_{in1}\rangle$ and $|\psi_{in2}\rangle$, are coherently combined into a single output mode $|\psi_{out}\rangle$, the resulting field can be written as $|\psi_{out}\rangle = \frac{1}{\sqrt{2}}(|\psi_{in1}\rangle + |\psi_{in2}\rangle)$, where the normalization factor ensures energy conservation. The corresponding output power is $P_{out} = |\psi_{out}|^2 = \frac{1}{2}|\psi_{in1}|^2 + \frac{1}{2}|\psi_{in2}|^2 + |\psi_{in1}||\psi_{in2}|cos(\phi)$, with ϕ denoting the relative phase between the two inputs. For two identical coherent sources, $|\psi_{in1}\rangle = |\psi_{in2}\rangle = |\psi_{in}\rangle$ and zero relative phase ($\phi = 0$), the output field amplitude becomes $|\psi_{out}| = \sqrt{2}|\psi_{in}|$, yielding an output power $P_{out} = 2P_{in}$ where P_{in} is the input power of each channel. This result encapsulates the fundamental principle of coherent addition: phase-aligned inputs combined constructively to enhance power.

The electric-field amplitude inside the waveguide was measured using directional couplers at the input and output ports for different angular positions, α, and recorded with a high-speed oscilloscope as shown in Fig. 6(c). Measurements were performed at two representative angular settings (red and green markers), revealing clear destructive interference at one extreme (red) and constructive interference at the other (green). At constructive interference, the measured input-to-output field ratio approaches the theoretical value of √2. The output power exhibits the expected cosine dependence on the relative phase, with a maximum power enhancement approaching a factor of two. The measured coherent combining efficiencies of two sources reach 98.9% at 2.88 GHz and 86.8% at 2.856 GHz as depicted in Fig. 6(c) and Fig. 6 (d), respectively.

To ensure measurement accuracy, the experimental setup was calibrated directly at the input ports of the power divider (P1 and P2) using a destructive interference nulling technique, guaranteeing equal field amplitudes at both ports. By utilizing this calibration to offset the intrinsic insertion losses of the phase shifter, residual interference

imperfections were isolated strictly to the phase and amplitude noise of the independent amplifiers. The analytical fit in Fig. 6(d) exhibits a 6.9° phase offset and a normalized amplitude of 0.9. Calculated from the raw data, the system's phase noise (0.05°) and relative amplitude noise (7%) yield a combining efficiency of >99% of the waveguide combiner; in agreement with the data presented in Fig. 6.

From these measurements we show brightness multiplication of the combined sources as $B_{out} = P_{out}/A_A = 2B_{in}$, where B_{in} is the input brightness of both sources, B_{out} is the output brightness, and A and $_A$ are the cross-section area and the solid angle of the waveguide mode, respectively. The brightness enhancement arises because the input and output modes share the same A_A product, a fundamental characteristic of coherent addition. This principle underpins scalable routes to high-power, high-brightness microwave radiation.

We propose and experimentally demonstrate a 2:1 combining scheme. For large-scale integration involving multiple sources, we advocate the use of cascaded 2:1 combiner rather than a single N:1 combiner. This approach offers improved robustness, as 2:1 combiner is less susceptible to single-source failures. In an N:1 configuration, the failure of one source may lead to complete output suppression and undesired reflections affecting the remaining sources. In contrast, our 2:1 combiner is designed and experimentally verified to deliver an output power of P/2 when only one input port is excited while the other remains unpowered as depicted in Fig. 6(e), thereby ensuring stable and predictable operation under partial failure conditions.

Together, these results demonstrate robust coherent addition of microwave sources enabled by the Berry-phase–based phase shifter, which provides precise phase control, broad bandwidth, and low insertion loss, large-scale integrable, while remaining compatible with high-power operation.

Discussion

We have experimentally demonstrated coherent combining of HPM radiation using a high-efficiency phase shifter that exploits a geometric (Berry) phase. By precisely manipulating the polarization state within a circular waveguide, the device enables controlled mode conversion and continuous phase tuning while sustaining operation in the HPM regime up to 2.3 MW without electrical breakdown. This performance highlights the robustness of geometric-phase control as an alternative to conventional electrically driven or mechanically tuned phase-shifting approaches in extreme-power environments.

Beyond the device demonstration, we introduced a generalized Bloch-sphere representation for waveguide polarization modes. This framework provides an intuitive yet rigorous description of mode evolution and phase accumulation in guided electromagnetic systems, revealing the geometric origin of the acquired phase. Such a representation unifies polarization, mode conversion, and phase control within a single analytical picture, offering new insight into electromagnetic interactions in waveguides.

The coherent addition strategy presented here, grounded in Berry-phase engineering, establishes a scalable route toward phase-stable HPM systems. Because the approach relies on passive dielectric structures rather than active electronic components, it is inherently compatible with high-power operation and reduced breakdown risk. More broadly, our results open a pathway toward HPM architectures based on dielectric metamaterials, where geometric-phase control may enable compact, efficient, and resilient platforms for high-power radiation generation and coherent combining.

Methods

Numerical simulations and metamaterial design

The design of the dielectric Berry-phase metasurface (BPM) waveplates was initiated using Effective Medium Theory (EMT). The initial geometrical parameters were analytically approximated by accounting for the guided

wavelength (λ_g) specific to the circular waveguide boundaries. Following this analytical estimation, full-wave finite-element frequency-domain (FEFD) simulations were employed to optimize the structure. The optimization target function prioritized equal transmission magnitudes along the fast and slow optical axes while achieving the exact desired phase retardation (90° for the QWP and 180° for the HWP) over a minimal propagation length. High-power breakdown endurance was computationally verified by simulating the spatial electric field distribution, ensuring peak electric fields remained well below the dielectric breakdown threshold of the pressurized gas environment.

Device fabrication and waveguide assembly

The circular waveguide components, featuring an inner diameter of 90 mm, were fabricated using high-precision computer numerical control (CNC) machining. The phase-shifting dielectric metamaterials were manufactured from alumina ceramic, characterized by a relative permittivity of $\epsilon_r = 9.9$ and a loss tangent of $\tan\delta = 0.001$, with strict fabrication tolerances of ± 0.1 mm to maintain modal purity. Rectangular-to-circular tapered waveguide transitions were utilized to couple the standard WR284 rectangular waveguide fundamental mode into the 90 mm circular waveguide TE_{11} mode. The coherent combining network incorporated a custom-designed 1:2 waveguide splitter/combiner and a commercial WR284 high-power circulator.

Low-power characterization

Initial phase retardation, mode conversion efficiency, and insertion loss were characterized in the low-power regime using a Vector Network Analyzer (VNA). Measurements were conducted utilizing a 10 mW continuous-wave (CW) source. This setup allowed for broadband frequency sweeping, identifying 2.88 GHz as the optimal operating frequency for the QWP retardation while providing a high-resolution phase measurement accuracy of 0.1°.

High-Power and coherent combining measurements

High-power durability tests were conducted using an RF source operating at a fixed frequency of 2.856 GHz. The system was driven with 5 µs pulses at a low repetition rate (20 to 50 Hz) to manage thermal loads and average energy consumption. To prevent dielectric RF breakdown—particularly at the sharp metamaterial-air interfaces—the waveguide system was sealed and pressurized with 10 psi (0.7 atm gauge) of sulfur hexafluoride (SF_6) gas. Electric-field amplitudes were sampled using directional couplers situated at the input and output ports of the combiner, and the signals were recorded via a high-speed oscilloscope.

Coherent combining and phase-locking stability tests were conducted using standard RF sources. Prior to the coherent addition measurements, the phase-shifted channels were carefully calibrated before the power divider; amplitude equalization was confirmed by tuning the phase shifter to achieve deep destructive interference at the output port, effectively nulling the residual signal and isolating the phase noise of the independent amplifiers.

Acknowledgements This work was supported by the PMRI – Peter Munk Research Institute – Technion and the PAZY foundation.

Author contributions G.G. conducted the experiment and wrote the manuscript. Y.O. contributed to the RF setup and Simulations. V.K provided manuscript feedback. E.M. and E.H. supervised the research. All authors reviewed the manuscript.

Funding The author received No Funding for this work.

Data availability All data supporting the findings of this study are available within the paper.

Declarations

Competing interests The authors declare no competing interests.

Open access I confirm that I understand Scientific Reports is an open access journal that levies an article processing charge per articles accepted for publication. By submitting my article I agree to pay this charge in full if my article is accepted for publication.

Dual Publication The results/data/figures in this manuscript have not been published elsewhere, nor are they under consideration (from you or one of your Contributing Authors) by another publisher.

Authorship I have read the Nature Portfolio journal policies on author responsibilities and submit this manuscript in accordance with those policies.

Third Party Material All of the material is owned by the authors and/or no permissions are required.

Open Access This article is licensed under a Creative Commons Attribution-NonCommercial-NoDerivatives 4.0 International License, which permits any non-commercial use, sharing, distribution and reproduction in any medium or format, as long as you give appropriate credit to the original author(s) and the source, provide a link to the Creative Commons licence, and indicate if you modified the licensed material. You do not have permission under this licence to share adapted material derived from this article or parts of it. The images or other third party material in this article are included in the article's Creative Commons licence, unless indicated otherwise in a credit line to the material. If material is not included in the article's Creative Commons licence and your intended use is not permitted by statutory regulation or exceeds the permitted use, you will need to obtain permission directly from the copyright holder. To view a copy of this licence, visit http://creativecommons.org/licenses/by-nc-nd/4.0/.

References

1. Sharypov, K. A. et al. Coherent summation of Ka-band microwave beams produced by sub-gigawatt superradiance backward wave oscillators. *Appl. Phys. Lett.* **103**, 134103. https://doi.org/10.1063/1.4823512 (2013).
2. Ju, J. et al. Coherent combining of phase-steerable high-power microwaves generated by two X-Band triaxial klystron amplifiers with pulsed magnetic fields. *Phys. Rev. Lett.* **130**, 085002. https://doi.org/10.1103/PhysRevLett.130.085002 (2023).
3. Shimshi, L. et al. Passive intra-cavity phase locking of laser channels. *Opt. Commun.* **263**, 60–64. https://doi.org/10.1016/j.optcom.2006.01.002 (2006).
4. Ishaaya, A. A., Davidson, N. & Friesem, A. A. Passive laser beam combining with intracavity interferometric combiners. *IEEE J. Sel. Top. Quantum Electron.* **15**, 301–311. https://doi.org/10.1109/JSTQE.2008.2010409 (2009).
5. Zhuang, Q. et al. A novel T-shaped high-power waveguide phase shifter with continuous linear phase adjustment. *Rev. Sci. Instrum.* **94**, 034704. https://doi.org/10.1063/5.0097739 (2023).
6. Cai, J. et al. A high-power S-band waveguide phase shifter with rotary RF chokes. *IEEE Microw. Wirel. Tech. Lett.* **34**, 383–386. https://doi.org/10.1109/LMWT.2024.3349976 (2024).
7. Chang, C. et al. A new compact high-power microwave phase shifter. *IEEE Trans. Microw. Theory Techn*. **63**, 1875–1882. https://doi.org/10.1109/TMTT.2015.2423281 (2015).
8. Berry, M. V. Quantal phase factors accompanying adiabatic changes. *Proc. R Soc. Lond. Ser. A*. **392**, 45–57. https://doi.org/10.1098/rspa.1984.0023 (1984).
9. Berry, M. V. The adiabatic phase and Pancharatnam's phase for polarized light. *J. Mod. Opt.* **34**, 1401–1407. https://doi.org/10.1080/09500348714551321 (1987).
10. Pancharatnam, S. Generalized theory of interference, and its applications, Part I. Coherent pencils. *Proc. Indian Acad. Sci. Sect. A*. **44**, 247–262. https://doi.org/10.1007/BF03046050 (1956).
11. Bliokh, K. Y., Rodríguez-Fortuño, F. J., Nori, F. & Zayats, A. V. Spin-orbit interactions of light. *Nat. Photonics*. **9**, 796–808. https://doi.org/10.1038/nphoton.2015.201 (2015).
12. Bomzon, Z., Kleiner, V. & Hasman, E. Pancharatnam-Berry phase in space-variant polarization-state manipulations with subwavelength gratings. *Opt. Lett.* **26**, 1424–1426. https://doi.org/10.1364/OL.26.001424 (2001).
13. Bomzon, Z., Biener, G., Kleiner, V. & Hasman, E. Space-variant Pancharatnam-Berry phase optical elements with computer-generated subwavelength gratings. *Opt. Lett.* **27**, 1141–1143. https://doi.org/10.1364/OL.27.001141 (2002).

14. Maguid, E. et al. Photonic spin-controlled multifunctional shared-aperture antenna array. *Science* **352**, 1202–1206. https://doi.org/10.1126/science.aaf3417 (2016).
15. Arbabi, A., Horie, Y., Bagheri, M. & Faraon, A. Dielectric metasurfaces for complete control of phase and polarization with subwavelength spatial resolution and high transmission. *Nat. Nanotechnol*. **10**, 937–943. https://doi.org/10.1038/nnano.2015.186 (2015).
16. Zheng, G. et al. Metasurface holograms reaching 80% efficiency. *Nat. Nanotechnol*. **10**, 308–312. https://doi.org/10.1038/nnano.2015.2 (2015).
17. Chong, K. E. et al. Polarization-independent silicon metadevices for efficient optical wavefront control. *Nano Lett.* **15**, 5369–5374. https://doi.org/10.1021/acs.nanolett.5b01752 (2015).
18. Wang, Q. et al. Optically reconfigurable metasurfaces and photonic devices based on phase change materials. *Nat. Photonics*. **10**, 60–65. https://doi.org/10.1038/nphoton.2015.247 (2016).
19. Yang, Z. et al. Asymmetric full-color vectorial meta-holograms empowered by pairs of exceptional points. *Nano Lett.* **24**, 844–851. https://doi.org/10.1021/acs.nanolett.3c03611 (2024).
20. Qin, H. et al. Disorder-assisted real–momentum topological photonic crystal. *Nature* **639**, 602–608. https://doi.org/10.1038/s41586-025-08632-9 (2025).
21. Ouyang, X. et al. Ultra narrowband geometric-phase resonant metasurfaces. *Proc. Natl. Acad. Sci. U S A*. **122**, e2420830122. https://doi.org/10.1073/pnas.2420830122 (2025).
22. Li, W. et al. Intelligent metasurface system for automatic tracking of moving targets and wireless communications based on computer vision. *Nat. Commun.* **14**, 989. https://doi.org/10.1038/s41467-023-36645-3 (2023).
23. Li, W. H. et al. An externally perceivable smart leaky-wave antenna based on spoof surface plasmon polaritons. *Opto-Electron Adv.* **7** https://doi.org/10.29026/oea.2024.240040 (2024).
24. Lin, Y. T. et al. High-Q geometric-phase metasurfaces for advanced light wavefront shaping. *Adv. Funct. Mater.* **35**, e2510521. https://doi.org/10.1002/adfm.202510521 (2025).
25. Li, W. et al. Stretchable Antenna Arrays-Enabled Multi-Target Balloon Wireless Communication System. *Adv. Funct. Mater.* **36**, e10521. https://doi.org/10.1002/adfm.202510521 (2026).
26. Li, L. et al. Multifunctional all-silicon terahertz chiral metasurfaces via integrated Moiré and spin-decoupled phase engineering. *Laser Photonics Rev.* **2503260** https://doi.org/10.1002/lpor.202503260 (2025).
27. Li, J. et al. Twisted bilayer meta-devices for on-demand terahertz polarization filtering. *Photon Res.* **13**, 1116–1129. https://doi.org/10.1364/PRJ.554358 (2025).
28. Wu, Y., Grant, P. S. & Isakov, D. 3D-printed λ/4 phase plate for broadband microwave applications. *Opt. Express*. **26**, 29068–29073. https://doi.org/10.1364/OE.26.029068 (2018).
29. Wu, J. et al. Nonuniform optical coherence engineering for the compact synthesis of robust higher-order Poincaré sphere beams. *ACS Photonics*. **13**, 335–341. https://doi.org/10.1021/acsphotonics.5c02564 (2026).
30. Toninelli, E. et al. Concepts in quantum state tomography and classical implementation with intense light: a tutorial. *Adv. Opt. Photon*. **11**, 67–134. https://doi.org/10.1364/AOP.11.000067 (2019).
31. Fox, A. G. An adjustable wave-guide phase changer. *Proc. IRE*. **35**, 1489–1498. https://doi.org/10.1109/JRPROC.1947.234574 (1947).
32. Bokor, N., Shechter, R., Davidson, N., Friesem, A. A. & Hasman, E. Achromatic phase retarder by slanted illumination of a dielectric grating with period comparable with the wavelength. *Appl. Opt.* **40**, 5040–5047. https://doi.org/10.1364/AO.40.002076 (2001).

Publisher's note Springer Nature remains neutral with regard to jurisdictional claims in published maps and institutional affiliations.

Authors and Affiliations

Gal Goldstein[1] · Yossi Oppenheim[1] · Vladimir Kleiner[1] · Erez Hasman[1] · Elhanan Maguid[1]

✉ Erez Hasman
mehasman@technion.ac.il

✉ Elhanan Maguid
selhanan@alumni.technion.ac.il

[1] Atomic-Scale Photonics Laboratory, Russell Berrie Nanotechnology Institute, Helen Diller Quantum Center, Technion – Israel Institute of Technology, Haifa, Israel